

Enhanced Phase-Change Condensation Using Inverse Opals

Solomon Adera (✉ sadera@umich.edu)

University of Michigan–Ann Arbor

Nikolaj K. Mandsberg

Technical University of Denmark

Lauren Naworski

Harvard University

Anna V. Shneidman

Harvard University

Jack Alvarenga

Harvard University

Joanna Aizenberg

Harvard University

Research Article

Keywords: Phase-change condensation, high surface energy, fabrication defects , visualization

Posted Date: February 15th, 2021

DOI: <https://doi.org/10.21203/rs.3.rs-195267/v1>

License: © ⓘ This work is licensed under a Creative Commons Attribution 4.0 International License.

[Read Full License](#)

Enhanced Phase-Change Condensation Using Inverse Opals

Solomon Adera,^{1,2,5,*} Nikolaj K. Mandsberg,⁴ Lauren Naworski,¹ Anna V. Shneidman,¹ Jack Alvarenga², Joanna Aizenberg^{1,2,3,*}

¹John A. Paulson School of Engineering and Applied Sciences, Harvard University, Cambridge, Massachusetts 02138, USA.

²Wyss Institute for Biologically Inspired Engineering, Harvard University, Cambridge, Massachusetts 02138, USA.

³Department of Chemistry and Chemical Biology, Harvard University, Cambridge, Massachusetts 02138, USA.

⁴Department of Micro- and Nanotechnology, Technical University of Denmark, 2800 Kongens Lyngby, Denmark

⁵Department of Mechanical Engineering, University of Michigan, Ann Arbor, Michigan 48109, USA.

Address correspondence to sadera@umich.edu and jaiz@seas.harvard.edu

Abstract

Phase-change condensation is commonplace in power and process engineering. Due to high surface energy, most condenser surfaces exhibit filmwise mode wherein the condensate is removed due to gravity when the weight overcomes pinning forces. Here, we use cracks (fabrication defects), which form when a copper tube is coated with inverse opals, to transport the condensate away from the condensing surface. Our visualization and experiments show that the cracks have high hydraulic conductivity that preferentially transports the condensate towards the ends of the copper tube. This improves the heat transfer coefficient to $\sim 80 \text{ kW/m}^2\cdot\text{K}$ from $\sim 12 \text{ kW/m}^2\cdot\text{K}$ for filmwise condensation on smooth copper tubes. Additionally, when the porous inverse opals are impregnated with a lubrication film, the heat transfer coefficient increases by an additional 30% to $103 \text{ kW/m}^2\cdot\text{K}$. Repeated experiments show that our material design is durable. The insights gained from this work informs the rational design of condenser surfaces.

Introduction

Vapor-to-liquid phase change condensation is routinely observed in numerous industrial processes.¹⁻¹¹ For example, in a fossil-fueled or nuclear-powered steam power plant (Rankine cycle), water is boiled in a boiler and steam/vapor is condensed in a condenser. In an oil-refinery, oil is evaporated in subsequent stages in a distillation tower to give a variety of vapor products, which are eventually condensed into liquid hydrocarbons such as benzene and kerosene. In multi-stage flash desalination plants, the vapor that is generated from saltwater (brine) by absorbing thermal energy is subsequently condensed to produce potable water. These are just few examples that show how pervasive condensation is in industrial processes. Condensation is also relevant in everyday life. We observe condensation when plant leaves collect dew on humid days. Condensation processes require that the enthalpy of phase change be removed by a working fluid or coolant. The enthalpy of phase change is particularly large for water (12.44 MJ/kg). Given the pervasiveness of phase-change condensation in everyday life and industry, enhancing condensation heat transfer is highly desired.

When a surface that is exposed to a vapor (hot steam) is cooled below the saturation temperature of the surrounding vapor, condensation occurs spontaneously on the surface. Depending on the wettability of the surface, vapor condenses by forming a continuous liquid film or discrete droplets. Due to the high surface energy, hydrophilic surfaces (for example, metals and their oxides) typically exhibit filmwise condensation.^{12,13} However, when the surface is hydrophobized by coating it with a promoter material (for example, silane treatment), vapor condenses in dropwise mode (discrete water droplets).¹⁴⁻¹⁶ Numerous studies have demonstrated that phase-change heat transfer during dropwise condensation is nearly an order of magnitude higher than filmwise condensation in a pure vapor environment since in the latter mode of condensation, the continuous liquid film adds a conduction resistance (thermal barrier) to heat transfer. Furthermore, during dropwise condensation, the periodic shedding of discrete water droplets when they reach the capillary length ($\approx 2.7 \text{ mm}$ for water at 25°C and 1 atm) improves the phase-change heat transfer rate by exposing the condensing surface to vapor in addition to refreshing active nucleation sites.

Hydrophobic coatings such as hydrocarbons and self-assembled monolayers,¹⁷⁻²¹ which are central in lowering the surface energy and forcing vapor to condense as discrete water droplets instead of a continuous liquid film, are not durable. Typical hydrophobic coatings last only few days or weeks depending on the working conditions such as vapor temperature and pressure inside the condenser. For example, Hampson & Ozisiks²² showed that a brass surface treated with oleic acid exhibits dropwise condensation for 7 days if the steam contains 0.1% nitrogen. In this study, the same surface lasted only ~3 h when the condenser surface was exposed to pure steam. Industrial condenser surfaces, however, are required to last longer than what have been reported thus far. Of course, thick hydrophobic coatings can last longer. But increasing coating thickness defeats the purpose since such approaches adds to the overall conduction resistance to heat transfer. Despite numerous studies since it was reported in the 1930s,²³ creating durable coatings that last for months and years has not been successful.

In this work, we demonstrate a different approach that does not require a hydrophobic coating. We coat the condensing surface with silica inverse opals that preferentially transport the condensate away from the condensing surface by providing a less resistant flow path for the condensate. Our material design provides a durable solution by avoiding the need for chemical functionalization (hydrophobic coating) altogether. We coated copper tubes with porous silica inverse opals to allow vapor to condense in its energy favorable state (filmwise mode) by making use of the inherent hydrophilicity of metals. Transporting the condensate away from the condensing surface through the crack (fabrication defects) improved the heat transfer rate in our experiments. The concept of thin-film condensation using porous structures has been reported in previous studies.²⁴⁻²⁹ The current work validates the concept by conducting heat transfer measurements and providing visual confirmation *via* environmental scanning electron microscopy (ESEM). The insights gained from this work inform material design for condenser surfaces that do not require hydrophobic coating and yet achieve high phase-change heat transfer rate. The results of this work present an opportunity to solve one of the long-standing durability concerns of modern condenser surfaces.

Sample fabrication

Using the bottom-up colloidal co-assembly technique,³⁰⁻³² we coated copper tubes (length = 60 mm, external diameter = 6.35 mm, internal diameter = 4.57 mm) with silica inverse opals; a highly porous material consisting of sub-micron voids in a support matrix (see materials and methods for material synthesis and sample fabrication). Typical scanning electron micrograph (SEM) images of the porous inverse opal coating at different magnifications are shown in Fig. 1a-d. During co-assembly of the sacrificial polystyrene beads (~395 nm diameter), the contact area that remained dry (*i.e.*, without being wetted by the solution) resulted in interconnected network of holes (~215 nm diameter) as can be seen in Fig. 1d. Based on our SEM measurements, typical thickness of the inverse opal coating was ~8-12 μm . Since silicon dioxide is intrinsically hydrophilic,³³ a water droplet spreads with vanishing contact angle (inset, Fig. 1a). Due to material shrinkage during the drying stage of our fabrication protocol, micro-cracks with large hydraulic conductivity (compared to the nanopores) formed between islands of inverse opals as shown in Fig. 1a-b. When the inverse opal coating is functionalized and impregnated with oil, the advancing/receding contact angle becomes 95°/94° (inset, Fig. 1c). Surface wettability characterization and additional SEM images taken post condensation experiment are provided in Supporting Material Section S1.

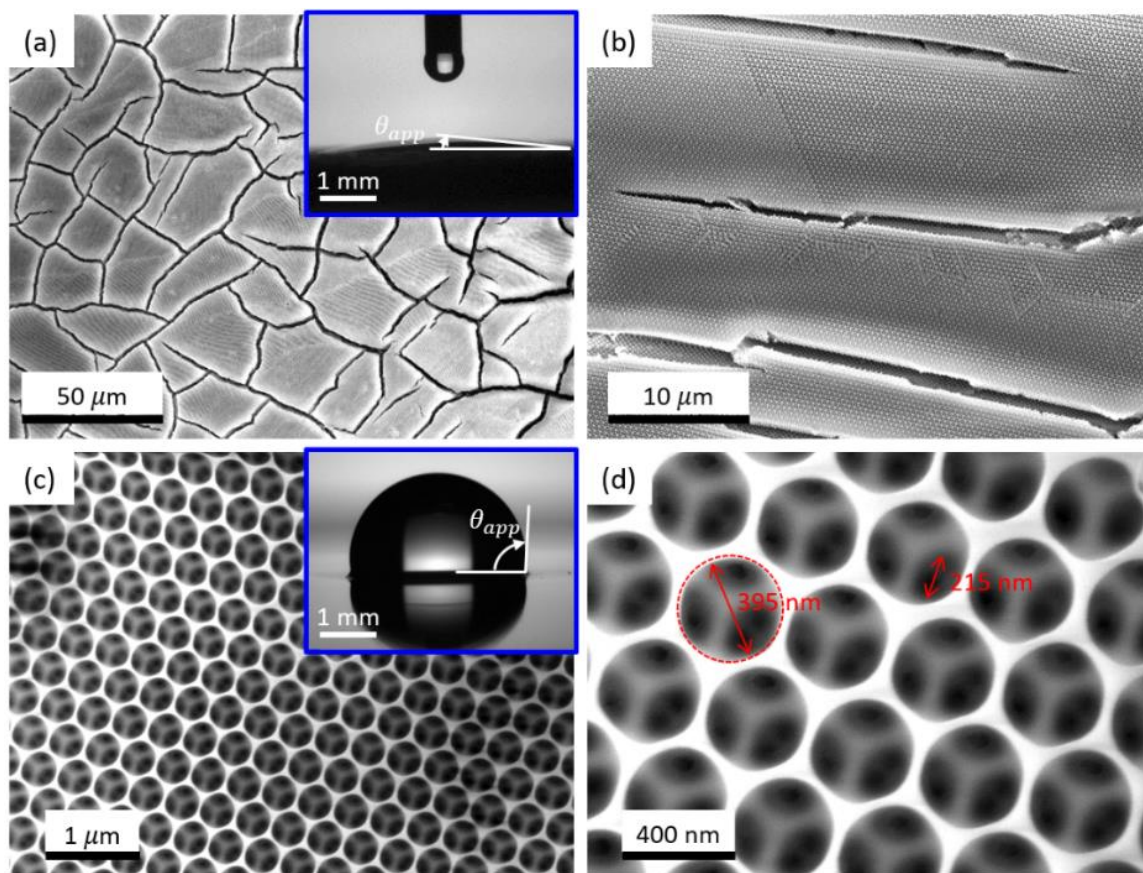


Figure 1. SEM at different magnifications. The low magnification SEM images in (a) and (b) show fabrication defects (cracks) that formed when the supporting matrix shrank during drying. The inset in (a) shows a vanishing (near zero) contact angle of a water droplet on a silica inverse opal coated copper plate. The high magnification images in (c) and (d) show the nanopores (~ 395 nm diameter) which are voids left behind by the sacrificial polystyrene beads. The contact points between the polystyrene beads that was not wetted by the solution during co-assembly created interconnected pores (~ 215 nm diameter). When the porous inverse opal coating was impregnated with a lubrication film, the advancing/receding contact angle became $95^\circ/94^\circ$ (inset c).

Results and discussion

We built an experimental setup which has three main components: environmental chamber, vapor generator, and cooling system (Fig. 2). In addition to maintaining the chamber at saturated conditions (saturated temperature and pressure), the stainless steel environmental chamber is designed to eliminate noncondensable gases (NCGs) from the system. NCGs, for example nitrogen, with concentrations as low as <10 ppm have been demonstrated to negatively impact phase-change heat transfer by creating a diffusion barrier for vapor transport.³⁴⁻⁴⁰ As a result, for reliable heat transfer measurements, condensation heat transfer measurements need to be conducted in a controlled environment where NCGs are absent. Details of the custom-made environmental chamber is presented in Supporting Material Section S2.

In preparation for the experiment, the water in the vapor generator was degassed *via* boiling. The degassed water in the vapor generator was maintained at saturated conditions at $\sim 85^\circ\text{C}$ and ~ 58 kPa. After attaching a copper tube to the cooling water circulation line, the entire system was evacuated using a roughing pump to remove NCGs. The absence of NCGs was confirmed by matching the chamber saturation temperature with the chamber vapor pressure.⁴¹ The copper tube was maintained below the chamber saturation temperature by circulating chilled water *via* the cooling system. During the experiment, hot steam (vapor) was allowed to enter the environmental chamber from the vapor generator by opening a valve. The vapor that entered the chamber condensed on the copper tube. All other tubings were insulated to avoid

condensation anywhere but the copper tube. The chamber was externally insulated to reduce heat loss to the surrounding environment. During the experiment, the walls of the chamber were slightly heated above saturation temperature by wrapping a rope heater externally. This was required to prevent condensation on the internal walls of the chamber which hindered visualization. Images of droplet nucleation, growth, and departure were captured at 0.2 frames per second (fps) using a DSLR camera.

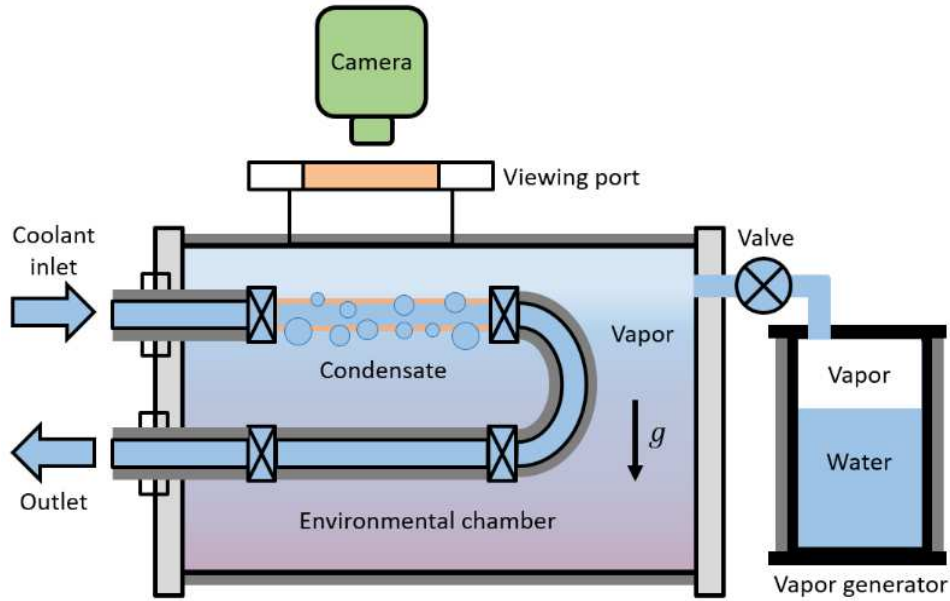


Figure 2. Schematic experimental setup. The chamber is insulated and condensation on the internal walls is prevented by slightly heating it above the saturation temperature. The water in the vapor generator was degassed prior to experiment and vapor was supplied to the chamber through a valve. The copper tube was maintained below the chamber temperature by circulating chilled water. The steam that entered the chamber was allowed to condense on the copper tube. Droplet nucleation, growth and departure phenomenon was captured at 0.2 fps using a DSLR camera.

Different modes of condensation ensue depending on surface functionalization (Fig. 3). When a smooth copper tube was plasma treated, steam condensed by forming a continuous liquid film in filmwise mode (Fig. 3a). As shown by the arrows in the time-lapse images in Fig. 3a, the condensate liquid film (filmwise condensation, FWC) continued to grow and became excessively large before falling vertically down when gravity overcame surface tension forces. However, when the smooth copper tube was hydrophobized *via* silane treatment, vapor condensed by forming discrete water droplets in dropwise mode (Fig. 3b). During dropwise condensation (DWC), droplets fall vertically down by overcoming surface tension when they reach the capillary length (≈ 2.7 mm for water). When the copper tube was coated with porous silica inverse opals, the condensate seeped into the interconnected nanopores since both the underlying copper and the silica inverse opals were inherently hydrophilic (high surface energy). Importantly, the condensate was transported away from the condensing surface towards the ends of the copper tube in the axial direction through the cracks (see arrows in Fig. 3c). In our experiments, the cracks or fabrication defects facilitated axial condensate transport by providing a less resistant flow path, that is, compared to the nanopores, the cracks have large hydraulic conductivity. This axial condensate transport mechanism is distinctively different from FWC and not reported in prior studies. Hereinafter, we refer to this mode of condensation as inverse opal condensation (IOC). When the porous inverse opals were chemically functionalized and impregnated with silicone oil (100 cSt at 25 °C, Sigma Aldrich), vapor condenses by forming highly mobile discrete water droplets that depart at smaller length scale as shown in Fig. 3d. Hereinafter, this mode of condensation on micro/nanostructured lubricated surfaces (*i.e.*, slippery liquid-infused porous surfaces or SLIPS) is referred to as SLIPS condensation or simply SLIPS. This surfaces are also referred as lubricant infused surfaces or LIS. Compared to the classical DWC, prior studies have shown that SLIPS condensation improves the heat transfer rate by reducing the departure radius by nearly 50%.⁴²⁻⁴⁷

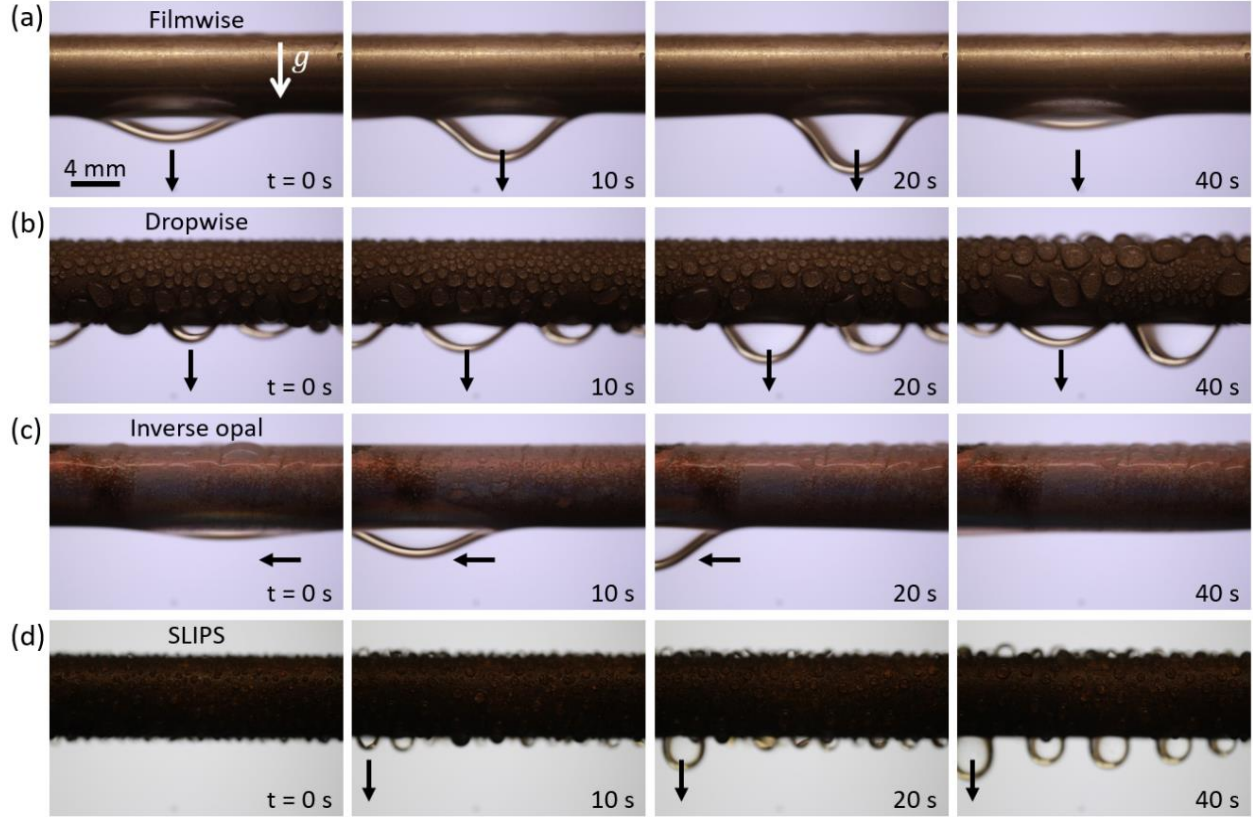


Figure 3. Modes of condensation. Time-lapse images of (a) filmwise condensation (FWC) on smooth plasma treated, (b) dropwise condensation (DWC) on smooth hydrophobized (silane treated), (c) inverse opal condensation (IOC) on silica inverse opals, and (d) SLIPS condensation on oil-impregnated silica inverse opals. In all cases except IOC, condensate was drained vertically downwards when gravity overcame pinning or surface tension forces. During IOC, however, the condensate was transported preferentially in the axial direction through the cracks (fabrication defects). Compared to nanopores, fabrication defects (cracks) provide a less-resistant flow path or high hydraulic conductivity for liquid transport.

During experiments, the copper tube was maintained below saturation temperature of the environmental chamber by circulating chilled water whose inlet and outlet temperatures were measured using calibrated thermocouples (Supporting Material Section S3). For reliable heat transfer measurements, a 0.2-2.5 °C temperature difference was maintained between incoming and outgoing cooling water by adjusting the flow rate using a valve. In addition to temperature of the cooling water, the wet-bulb and dry-bulb temperatures, flow rate and chamber pressure were measured and recorded using a data acquisition system.

Since our experiments were neither constant temperature (isothermal) nor constant heat flux (isoflux), we used logarithmic mean for the average temperature difference between the condensing wall and surrounding vapor. For the inlet (T_1) and outlet (T_2) cooling water temperatures and chamber temperature (T_v), the logarithmic mean temperature difference is defined as $\Delta T_{LMTD} = (T_2 - T_1) / \ln(\Delta T_2 / \Delta T_1)$ where $\Delta T_2 = T_2 - T_v$ and $\Delta T_1 = T_1 - T_v$. The heat rejected by the steam per unit area (heat flux, q'') was calculated from internal flow analysis, that is, the heat released by the vapor during phase-change was carried away by the circulating chilled water. All data were acquired at steady-state conditions where all temperature fluctuation (wet-bulb, dry-bulb, inlet and outlet) and pressure fluctuations were ≤ 0.25 °C/min and ≤ 0.1 kPa/min, respectively. Steady-state data was time-averaged to yield a single data point shown in Fig. 4 (see Supporting Material Section S4 for detailed data reduction steps).

The heat flux as a function of logarithmic mean temperature for the different modes of condensation is shown in Fig. 4a. The smooth copper tube was plasma cleaned for FWC whereas it was silane treated for

DWC. Both DWC and IOC perform better than FWC. Among the different modes of condensation, SLIPS condensation performed the best since it removed high heat fluxes at small logarithmic mean temperature difference (Fig. 4a). The slope of heat flux versus logarithmic mean temperature difference is the heat transfer coefficient (h_c), which is a measure of the heat removed per unit area per unit temperature difference between wall and surrounding vapor.⁴⁸ The heat transfer coefficient as a function of the logarithmic mean temperature difference for the different modes of condensation is shown in Fig. 4b. In our measurements, the heat transfer coefficient for DWC and IOC were nearly identical (within measurement uncertainty) at 79 ± 14 kW/m²·K and 78 ± 17 kW/m²·K, respectively. This is nearly a sevenfold increase from FWC (12 ± 6 kW/m²·K). We attribute the high heat transfer rates in IOC to enhanced axial condensate transport through cracks (less resistant hydraulic path). Importantly, when the condensation experiments were repeated numerous times (>15 times), the inverse opal coated copper tubes maintained their high heat transfer rate (~ 80 kW/m²·K) whereas the silane coated copper tubes resorted to filmwise condensation after 5-8 experiments. This result shows that while hydrophobic coatings wear off quickly, the porous inverse opal structures remain attached on the copper tube after repeated experiments. We confirmed this by capturing SEM images of the copper tube after >15 condensation experiments, each experiment lasting 3-4 hr. Post condensation SEM images are shown in Supporting Material Section S1. Our material design, which allowed vapor to condense in its natural (energy favorable) state, addresses the major durability concern (wear and tear) of hydrophobic coatings while maintaining heat transfer rates comparable to DWC. Furthermore, when the porous inverse opal was impregnated with a lubrication film, the phase-change heat transfer coefficient increased by an additional 30% to 103 ± 13 kW/m²·K. We attribute the improvements in heat transfer to smaller droplet departure radius and higher droplet departure frequency on micro/nanostructured lubricated surfaces.^{42-44,46,49} The solid-liquid composite material design in SLIPS enhances droplet mobility (~ 1 -2° contact angle hysteresis) by providing an atomically smooth and chemically homogeneous liquid-liquid interface. We validated our heat transfer measurements by comparing the heat transfer coefficient for FWC with the classical Nusselt model (Supporting Material S5) for laminar filmwise condensation (red dashed line, Fig. 4b).⁵⁰ The error bars in Fig. 4 are calculated through error propagation analysis by combining systematic and random errors for one standard deviation (Supporting Material Section S6).

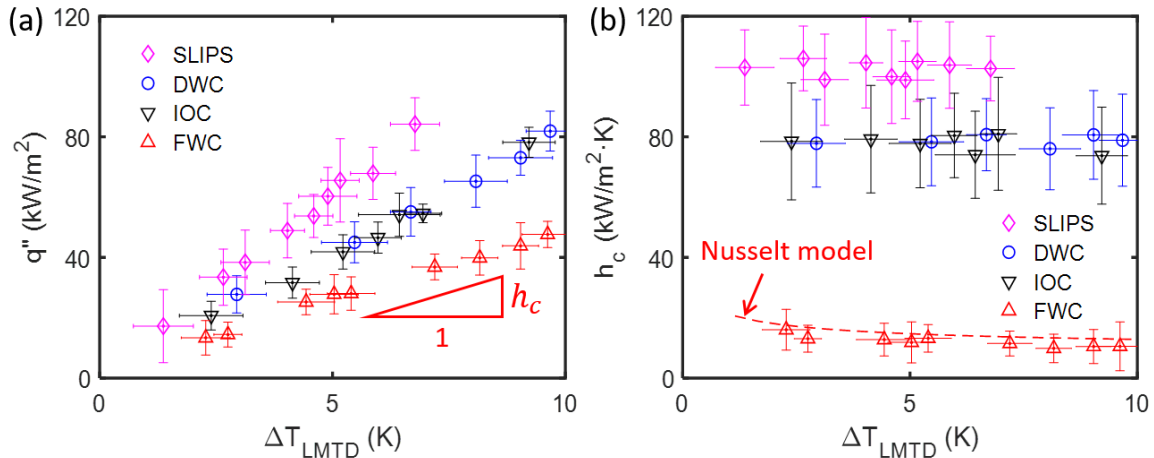


Figure 4. Heat transfer measurement. (a) Heat flux and (b) heat transfer coefficient as a function of logarithmic mean temperature difference. The slope in (a) is the heat transfer coefficient (h_c). The heat transfer coefficient for DWC and IOC are nearly identical at ~ 80 kW/m²·K; a sevenfold increase from FWC (~ 12 kW/m²·K). The heat transfer coefficient increases further by $\sim 30\%$ to ~ 103 kW/m²·K when the silica nanopores are impregnated with oil (SLIPS condensation). Our heat transfer measurements are validated by comparing the heat transfer coefficient for FWC with the classical Nusselt model for laminar film condensation (red dashed line). The error bars are obtained through standard error propagation analysis.

In addition to heat transfer measurements, we visualized phase-change condensation using an environmental scanning electron microscope (ESEM) (EVO 50 ESEM, Carl Zeiss Microscopy GmbH). For this *in-situ* characterization, the ESEM was maintained at saturated conditions at 7.4 °C and 1015 Pa. After securely attaching the test sample to a water-cooled Peltier stage (Deben TM-1000 Coolstage, Deben UK Limited) using a vacuum compatible carbon tape, the chamber was evacuated to remove NCGs. The cold stage was maintained 2 °C below the chamber saturation temperature. Backscatter detection mode (CZ-BSD) with high gain and a 25 kV beam potential was used for visualization/imaging. The probe current was maintained at ≤ 2.0 nA to suppress evaporation induced by laser power. To improve visualization, a 500 μm fixed pressure lower aperture was aligned in series with a 1000 μm variable pressure upper aperture. Using the built-in camera, images of droplet nucleation and growth were captured at 10 fps.

The time-lapse images in Fig. 5 show that droplet nucleation starts preferentially near fabrication defects. The cracks which were empty at $t = 0$ started to fill with condensate water at $t = 32$ s. When condensation continued, the condensate liquid started to overflow from the cracks as shown in the time-lapse images at $t = 44$ s and $t = 74$ s. When vapor supply was discontinued, the condensate that filled the cracks receded into the interconnected pores ($t = 88$ s). Eventually, the surface dried out at $t = 92$ s when all the condensate seeped into the porous structure and drained through the cracks. Faster condensate removal through the cracks refreshed the surface and prepared it for renewed droplet nucleation and growth. These results suggest that hierarchical (two-level) porosity, which can be achieved by engineering cracks in colloidal crystals,³² has a potential for faster condensate removal that can translate to improved phase-change condensation heat transfer rate.

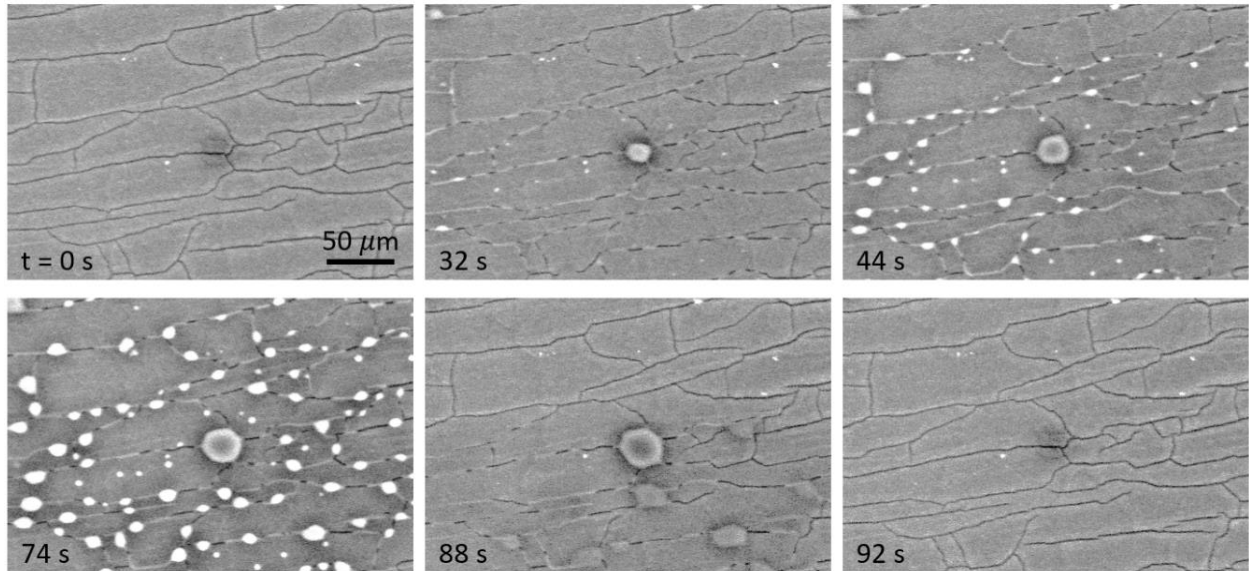


Figure 5. Environmental SEM. The ESEM was maintained at 7.4 °C and 1015 Pa. The test sample was attached to a cold stage that was subcooled by 2 °C. Time-lapse images (10 fps) show that vapor condensed preferentially near cracks ($t = 32$ s and 44 s). When condensation continued, the condensate overflowed ($t = 74$ s). The condensate was transported through the cracks ($t = 88$ s) and the surface dried out ($t = 92$ s) when vapor supply was discontinued.

Conclusions

In summary, we coated copper tubes with silica inverse opals ($\sim 8\text{--}12$ μm thickness) and characterized the phase-change heat transfer rate. Our material design does not require a hydrophobic coating; instead it takes advantage of the hydrophilicity of metals by allowing vapor to condense in its natural (energy favorable) state. Importantly, our material design allowed preferential condensate transport in the axial direction

towards the ends of the tube. This is distinct from filmwise and dropwise condensation wherein the condensate grows excessively large and falls vertically downwards when gravity overcomes surface tension forces. In our material design, faster condensate transport through the cracks (fabrication defects) clears the surface and rejuvenates the active nucleation sites. By providing a lesser resistance to condensate transport than the silica nanopores, the cracks improve condensation heat transfer rate. In our measurements, which is validated for filmwise mode using the classical Nusselt model, the heat transfer coefficient for inverse opal condensation was $\sim 80 \text{ kW/m}^2\cdot\text{K}$; a sevenfold increase from filmwise condensation. Importantly, when the steam condensation experiments were repeated >15 with each experimental run lasting 3–4 hr, our silica inverse opals remained attached on the copper tube and maintained the high heat transfer rates ($\sim 80 \text{ kW/m}^2\cdot\text{K}$), indicating enhanced durability compared to state-of-the-art hydrophobic coatings. Our *in-situ* ESEM visualization shows that condensate droplets that form preferentially near fabrication defects are transported through the cracks. When the nanopores were impregnated with a chemically matched lubrication film, the heat transfer coefficient increased further by an additional 30% to $103 \text{ kW/m}^2\cdot\text{K}$. By utilizing the innate wetting behavior of metals, our approach achieves high heat transfer rates that are comparable to dropwise condensation. The insights gained from this work can be used to rationally design durable condenser surfaces for industrial applications.

Materials and methods

Colloidal suspension

Colloidal suspension composed of 0.5 wt% colloids (395 nm diameter –COOH terminated polystyrene spheres), 0.1 wt% hydrolyzed tetraethoxy silane solution (TEOS, $\text{Si}(\text{OC}_2\text{H}_5)_4$) and 99.4 wt% de-ionized water (DIW) was prepared. The hydrolyzed TEOS solution was prepared by mixing TEOS, ethanol, and 0.1M hydrochloric acid (HCl) at 1:1:1 ratio. The solution was thoroughly mixed by stirring it for 24 h using a magnetic stirrer at 550 rev/min (rpm). Finally, the solution was added to the colloidal suspension before inserting the 15 min plasma treated copper tubes inside the solution for colloidal co-assembly.

Silica inverse opals

Copper tubes (length = 60 mm, external diameter = 6.35 mm, internal diameter = 4.57 mm) were sonicated (Branson M8800, Thermo Fisher Scientific) in an acetone bath for 15 min. This was followed by sequential cleaning using acetone, methanol, isopropanol (IPA), de-ionized water (DIW) and blow-drying with compressed air. Next, the copper tubes were coated with silicon dioxide (SiO_2) *via* atomic layer deposition (ALD) (50 cycles at 250°C , $\sim 50 \text{ nm}$ thickness). During ALD, the tubes were lifted slightly on one end by a metal wire to ensure uniform coverage. After ALD, the copper tubes were plasma treated (PE-200, Plasma Etch) for 15 min and immersed in a 12 ml glass vial filled with colloidal suspension. The assembly was placed in a constant temperature (65°C) convection oven on a vibration free table. After allowing the solution to evaporate fully for >3 days, the colloidal coated copper tubes were taken out of the oven and immersed in a toluene solution ($\text{C}_6\text{H}_5\text{CH}_3$, Sigma Aldrich) for $>24 \text{ h}$ to dissolve the sacrificial polystyrene beads. Typical thickness of the porous silica inverse opal coating left behind on the copper tubes was $\sim 8\text{--}12 \mu\text{m}$ based on our SEM.

Hydrophobization (silane deposition)

The inverse opal coated copper tubes were plasma treated for $\sim 15 \text{ min}$. Immediately after plasma treatment, the tubes were placed inside a transparent polycarbonate container (2204K5, McMaster-Carr) along with few drops of silane (trichloro(1H,1H,2H,2H-perfluorooctyl)silane) in a 35×10 polystyrene petri dish (Falcon™ 351008, Thermo Fisher Scientific). The pressure in the polycarbonate container was lowered by connecting it to a vacuum/suction line. Once low pressure (vacuum) was established inside the container, silane started to evaporate at which point the vacuum line was disconnected. Intermittently, the vacuum line was reconnected to allow all the liquid silane to evaporate. The evaporated silane in vapor phase was adsorbed on the plasma treated surface and rendered the copper tube hydrophobic.

Oil impregnation (SLIPS)

The inverse opal coated and hydrophobized copper tube was impregnated with a chemically matched silicone oil (100 cSt at 25 °C, Sigma Aldrich). After impregnation, the tube was oriented vertically upwards for >12 h to drain the excess lubrication oil *via* gravity. The lubrication oil that infiltrated the nanopores was immobilized by capillary forces. The lubricated tube was inspected visually for the absence of excess oil prior to experiment.

References

- 1 Beér, J. M. High Efficiency Electric Power Generation: The Environmental Role. *Prog. Energy Combust. Sci.* **33**, 107-134 (2007).
- 2 Hung, T.-C., Shai, T. & Wang, S. K. A review of organic Rankine cycles (ORCs) for the recovery of low-grade waste heat. *Energy* **22**, 661-667 (1997).
- 3 Reifert, V., Sardak, A., Grigorenko, S. & Podbereznyj, V. Heat Exchange at Dropwise Condensation in Heat Exchangers of Desalination Plants. *Desalination* **74**, 373-382 (1989).
- 4 Luijten, C., Van Hooy, R., Janssen, J. & Van Dongen, M. Multicomponent nucleation and droplet growth in natural gas. *J. Chem. Phys.* **109**, 3553-3558 (1998).
- 5 Khawaji, A. D., Kutubkhanah, I. K. & Wie, J.-M. Advances in seawater desalination technologies. *Desalination* **221**, 47-69 (2008).
- 6 Humplik, T. *et al.* Nanostructured materials for water desalination. *Nanotechnology* **22**, 292001 (2011).
- 7 Boreyko, J. B. & Chen, C.-H. Self-Propelled Dropwise Condensate on Superhydrophobic Surfaces. *Phys. Rev. Lett.* **103**, 184501-184504 (2009).
- 8 Boreyko, J. B., Zhao, Y. & Chen, C.-H. Planar jumping-drop thermal diodes. *Appl. Phys. Lett.* **99**, 234105 (2011).
- 9 Pérez-Lombard, L., Ortiz, J. & Pout, C. A Review on Buildings Energy Consumption Information. *Energy Build.* **40**, 394-398 (2008).
- 10 Peters, T. B. *et al.* Design of an Integrated Loop Heat Pipe Air-Cooled Heat Exchanger for High Performance Electronics. *IEEE Trans. Compon., Packag., Manuf. Technol.* **2**, 1637-1648 (2012).
- 11 Li, J., Lin, F., Wang, D. & Tian, W. A loop-heat-pipe heat sink with parallel condensers for high-power integrated LED chips. *Appl. Therm. Eng.* **56**, 18-26 (2013).
- 12 Sparrow, E. M. & Gregg, J. L. A Boundary-Layer Treatment of Laminar-Film Condensation. *J. Heat Transfer* **81**, 13-18 (1959).
- 13 Shekrladze, I. G. & Gomelaury, V. Theoretical Study of Laminar Film Condensation of Flowing Vapour. *Int. J. Heat Mass Transfer* **9**, 581-591 (1966).
- 14 Le Fevre, E. & Rose, J. An Experimental Study of Heat Transfer by Dropwise Condensation. *Int. J. Heat Mass Transfer* **8**, 1117-1133 (1965).
- 15 Tanaka, H. A Theoretical Study of Dropwise Condensation. *J. Heat Transfer* **97**, 72-78 (1975).
- 16 Wilke, K. L. *et al.* Polymer Infused Porous Surfaces for Robust, Thermally Conductive, Self-Healing Coatings for Dropwise Condensation. *ACS Nano* **14**, 14878-14886 (2020).
- 17 Blackman, L., Dewar, M. & Hampson, H. An investigation of compounds promoting the dropwise condensation of steam. *J. Appl. Chem.* **7**, 160-171 (1957).
- 18 Marto, P., Looney, D., Rose, J. & Wanniarachchi, A. Evaluation of organic coatings for the promotion of dropwise condensation of steam. *Int. J. Heat Mass Transfer* **29**, 1109-1117 (1986).
- 19 Vemuri, S. & Kim, K. An experimental and theoretical study on the concept of dropwise condensation. *Int. J. Heat Mass Transfer* **49**, 649-657 (2006).
- 20 Das, A., Kilty, H., Marto, P., Andeen, G. & Kumar, A. The use of an organic self-assembled monolayer coating to promote dropwise condensation of steam on horizontal tubes. *J. Heat Transfer* **122**, 278-286 (2000).
- 21 Kim, S. & Kim, K. J. Dropwise condensation modeling suitable for superhydrophobic surfaces. *J. Heat Transfer* **133**, 0815021-0815028 (2011).
- 22 Hampson, H. & Özişik, N. An investigation into the condensation of steam. *Proc. Instn. Mech. Engrs.* **167**, 282-294 (1952).

- 23 Schmidt, E., Schurig, W. & Sellschopp, W. Versuche über die Kondensation von Wasserdampf in Film-und Tropfenform. *Forsch. Ingenieurwes.* **1**, 53-63 (1930).
- 24 Oh, J. *et al.* Thin film condensation on nanostructured surfaces. *Adv. Funct. Mater.* **28**, 1707000-1707009 (2018).
- 25 Wang, R. & Antao, D. S. Capillary-Enhanced Filmwise Condensation in Porous Media. *Langmuir* **34**, 13855-13863 (2018).
- 26 Preston, D. J. *et al.* Gravitationally Driven Wicking for Enhanced Condensation Heat Transfer. *Langmuir* **34**, 4658-4664 (2018).
- 27 Degan, G., Sanya, A. & Akowanou, C. Laminar film condensation along a vertical plate embedded in an anisotropic porous medium with oblique principal axes. *Heat Mass Transfer* **52**, 2119-2128 (2016).
- 28 Sanya, A. S., Akowanou, C., Sanya, E. A. & Degan, G. Liquid film condensation along a vertical surface in a thin porous medium with large anisotropic permeability. *SpringerPlus* **3**, 659-668 (2014).
- 29 Al-Nimr, M. & Alkam, M. Film condensation on a vertical plate imbedded in a porous medium. *Applied Energy* **56**, 47-57 (1997).
- 30 Hatton, B., Mishchenko, L., Davis, S., Sandhage, K. H. & Aizenberg, J. Assembly of large-area, highly ordered, crack-free inverse opal films. *Proc. Natl. Acad. Sci. U. S. A.* **107**, 10354-10359 (2010).
- 31 Mishchenko, L., Hatton, B., Kolle, M. & Aizenberg, J. Patterning hierarchy in direct and inverse opal crystals. *Small* **8**, 1904-1911 (2012).
- 32 Phillips, K. R. *et al.* Fabrication of photonic microbricks via crack engineering of colloidal crystals. *Adv. Funct. Mater.* **30**, 1908242-1908211 (2020).
- 33 Raj, R., Maroo, S. C. & Wang, E. N. Wettability of graphene. *Nano Lett.* **13**, 1509-1515 (2013).
- 34 Huang, J., Zhang, J. & Wang, L. Review of vapor condensation heat and mass transfer in the presence of non-condensable gas. *Appl. Therm. Eng.* **89**, 469-484 (2015).
- 35 Ma, X.-H., Zhou, X.-D., Lan, Z., Yi-Ming, L. & Zhang, Y. Condensation heat transfer enhancement in the presence of non-condensable gas using the interfacial effect of dropwise condensation. *Int. J. Heat Mass Transfer* **51**, 1728-1737 (2008).
- 36 Peterson, P., Schrock, V. & Kageyama, T. Diffusion layer theory for turbulent vapor condensation with noncondensable gases. *J. Heat Transfer* **115**, 998-1003 (1993).
- 37 Corradini, M. L. Turbulent condensation on a cold wall in the presence of a noncondensable gas. *Nucl. Technol.* **64**, 186-195 (1984).
- 38 Kroger, D. G. & Rohsenow, W. M. Condensation heat transfer in the presence of a non-condensable gas. *Int. J. Heat Mass Transfer* **11**, 15-26 (1968).
- 39 Minkowycz, W. & Sparrow, E. Condensation heat transfer in the presence of noncondensables, interfacial resistance, superheating, variable properties, and diffusion. *Int. J. Heat Mass Transfer* **9**, 1125-1144 (1966).
- 40 Bum-Jin, C., Sin, K., Chan, K. M. & Ahmadinejad, M. Experimental comparison of film-wise and drop-wise condensations of steam on vertical flat plates with the presence of air. *Int. Comm. Heat Mass Transfer* **31**, 1067-1074 (2004).
- 41 Bejan, A. *Advanced Engineering Thermodynamics*. 3rd edn, (Wiley, 2006).
- 42 Xiao, R., Miljkovic, N., Enright, R. & Wang, E. N. Immersion Condensation on Oil-Infused Heterogeneous Surfaces for Enhanced Heat Transfer. *Sci. Rep.* **3**, 1988-1993 (2013).
- 43 Anand, S., Paxson, A. T., Dhiman, R., Smith, J. D. & Varanasi, K. K. Enhanced Condensation on Lubricant-Impregnated Nanotextured Surfaces. *ACS Nano* **6**, 10122-10129 (2012).
- 44 Sett, S. *et al.* Stable Dropwise Condensation of Ethanol and Hexane on Rationally Designed Ultrascable Nanostructured Lubricant-Infused Surfaces. *Nano Lett.* **19**, 5287-5296 (2019).
- 45 Preston, D. J. *et al.* Heat Transfer Enhancement during Water and Hydrocarbon Condensation on Lubricant Infused Surfaces. *Sci. Rep.* **8**, 540-548 (2018).
- 46 Adera, S. *et al.* Depletion of Lubricant from Nanostructured Oil-Infused Surfaces by Pendant Condensate Droplets. *ACS Nano* **14**, 8024-8035 (2020).

- 47 Kajiya, T., Schellenberger, F., Papadopoulos, P., Vollmer, D. & Butt, H.-J. 3D Imaging of Water-Drop Condensation on Hydrophobic and Hydrophilic Lubricant-Impregnated Surfaces. *Sci. Rep.* **6**, 23687-23696 (2016).
- 48 Mills, A. F. *Basic Heat and Mass Transfer*. 2nd edn, (Prentice-Hall, 1999).
- 49 Rykaczewski, K. *et al.* Dropwise Condensation of Low Surface Tension Fluids on Omniphobic Surfaces. *Sci. Rep.* **4**, 4158-4165 (2015).
- 50 Nusselt, W. Die Oberflächenkondensation des Wasserdampfes. *Zeitschrift Des Vereines Deutscher Ingenieure* **60**, 541-546 (1916).

Acknowledgements

The work is supported by the Office of Naval Research, U.S. Department of Defense, under Grant No. N00014-17-1-2913, NSF Materials Research Science and Engineering Center (MRSEC) at Harvard University under Award No. DMR 1420570 and Advanced Research Projects Agency-Energy, U.S. Department of Energy, under Award No. DE-AR0000326. We acknowledge the use of the facilities at the Harvard Center for Nanoscale Systems supported by the NSF under Grant No. ECS-0335765. N.K.M. is supported by the Fulbright, Danmark-Amerika Fondet, Weibel Scientific, Augustinus Fonden, and an Excellence PhD Scholarship from DTU Health Tech. S.A. would like to thank Prof. Michael J. Aziz and Dr. Diana De Porcellinis for allowing equipment use.

Author contributions

S. A. and J. Aizenberg conceived the idea and planned the experiments. J. Aizenberg guided the work. All authors contributed in designing the experiment and writing the manuscript.

Additional Information

Supporting information accompanies this paper at <https://doi.org/>

Competing interests: The authors declare that they have no competing interests.

Data and material availability. All data generated or analyzed during this study are included in this published article and/or the Supplementary material.

Figures

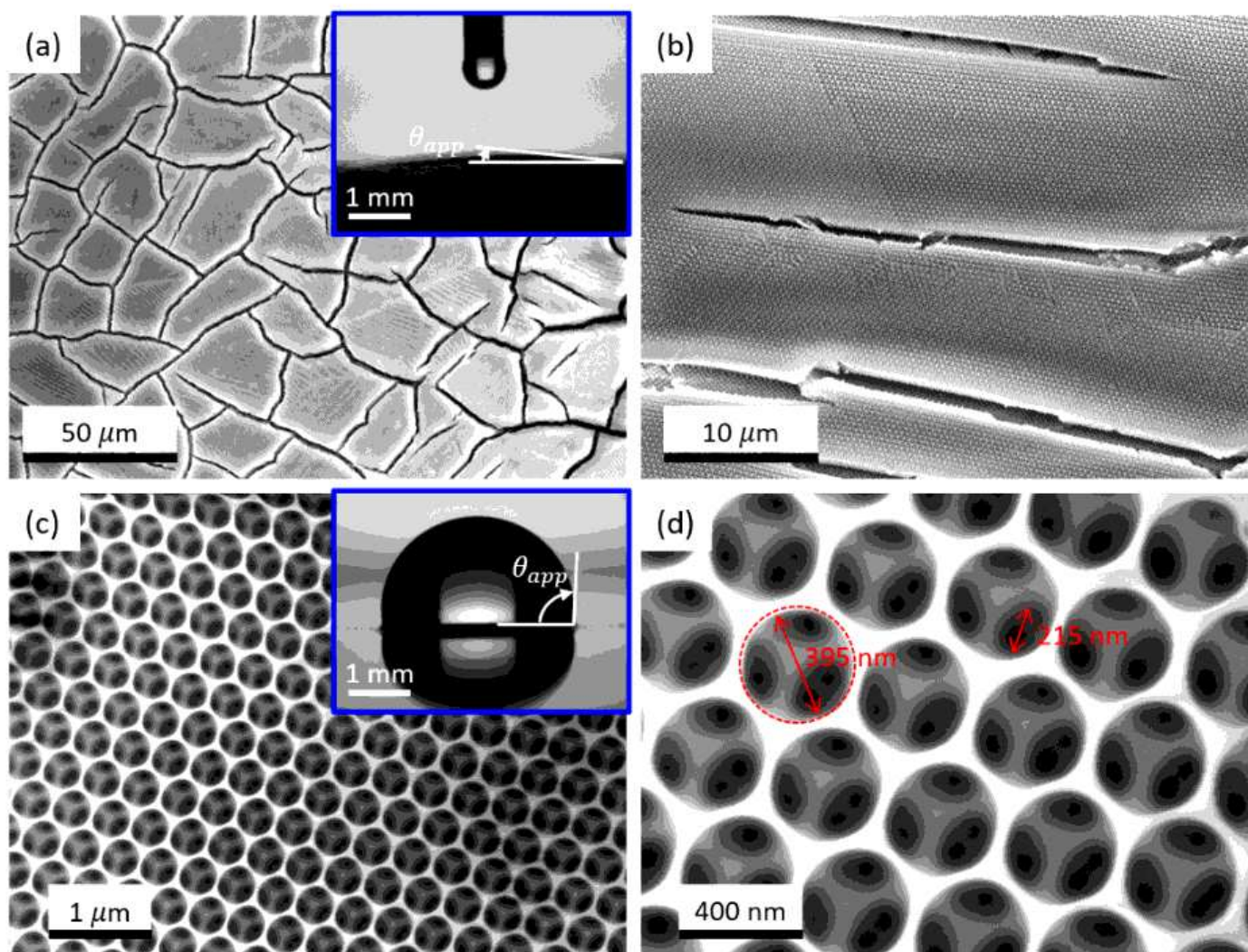


Figure 1

SEM at different magnifications. The low magnification SEM images in (a) and (b) show fabrication defects (cracks) that formed when the supporting matrix shrank during drying. The inset in (a) shows a vanishing (near zero) contact angle of a water droplet on a silica inverse opal coated copper plate. The high magnification images in (c) and (d) show the nanopores (~ 395 nm diameter) which are voids left behind by the sacrificial polystyrene beads. The contact points between the polystyrene beads that was not wetted by the solution during co-assembly created interconnected pores (~ 215 nm diameter). When the porous inverse opal coating was impregnated with a lubrication film, the advancing/receding contact angle became $95^\circ/94^\circ$ (inset c).

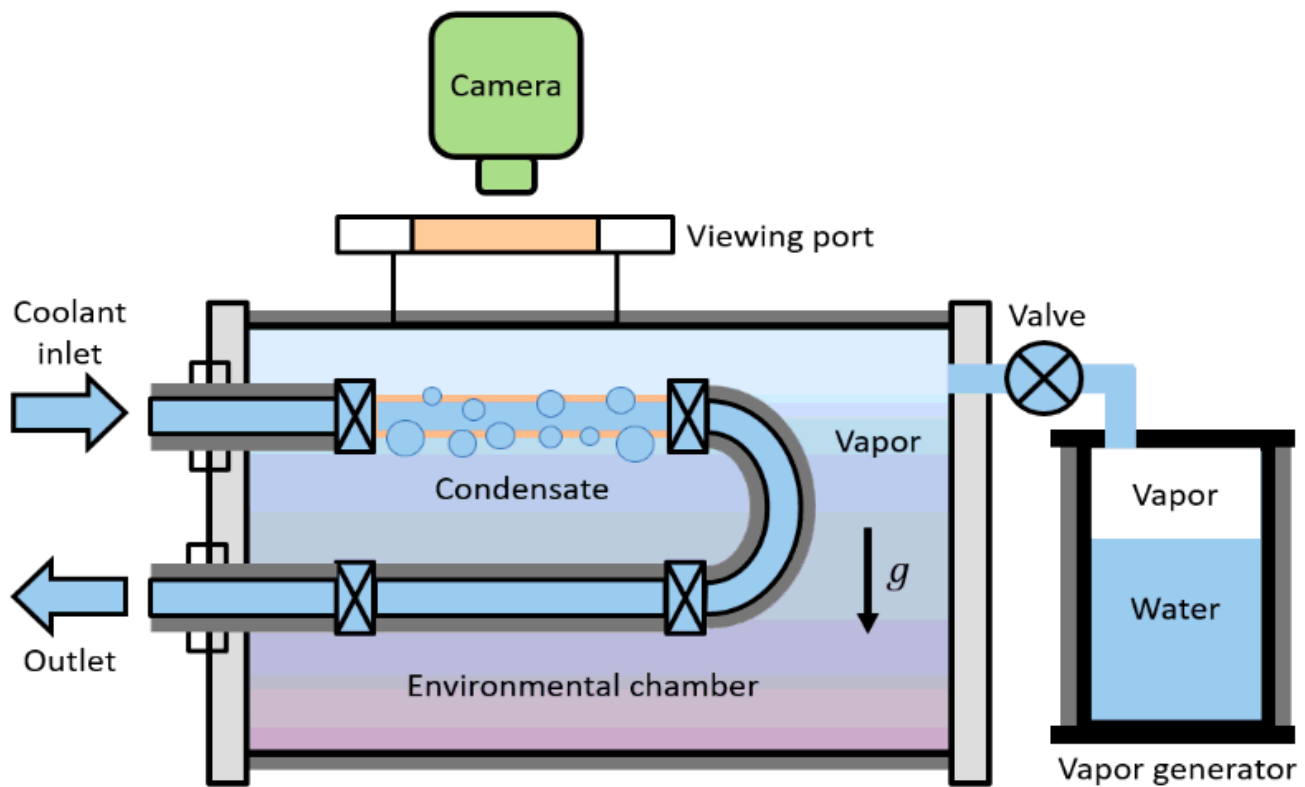


Figure 2

Schematic experimental setup. The chamber is insulated and condensation on the internal walls is prevented by slightly heating it above the saturation temperature. The water in the vapor generator was degassed prior to experiment and vapor was supplied to the chamber through a valve. The copper tube was maintained below the chamber temperature by circulating chilled water. The steam that entered the chamber was allowed to condense on the copper tube. Droplet nucleation, growth and departure phenomenon was captured at 0.2 fps using a DSLR camera.

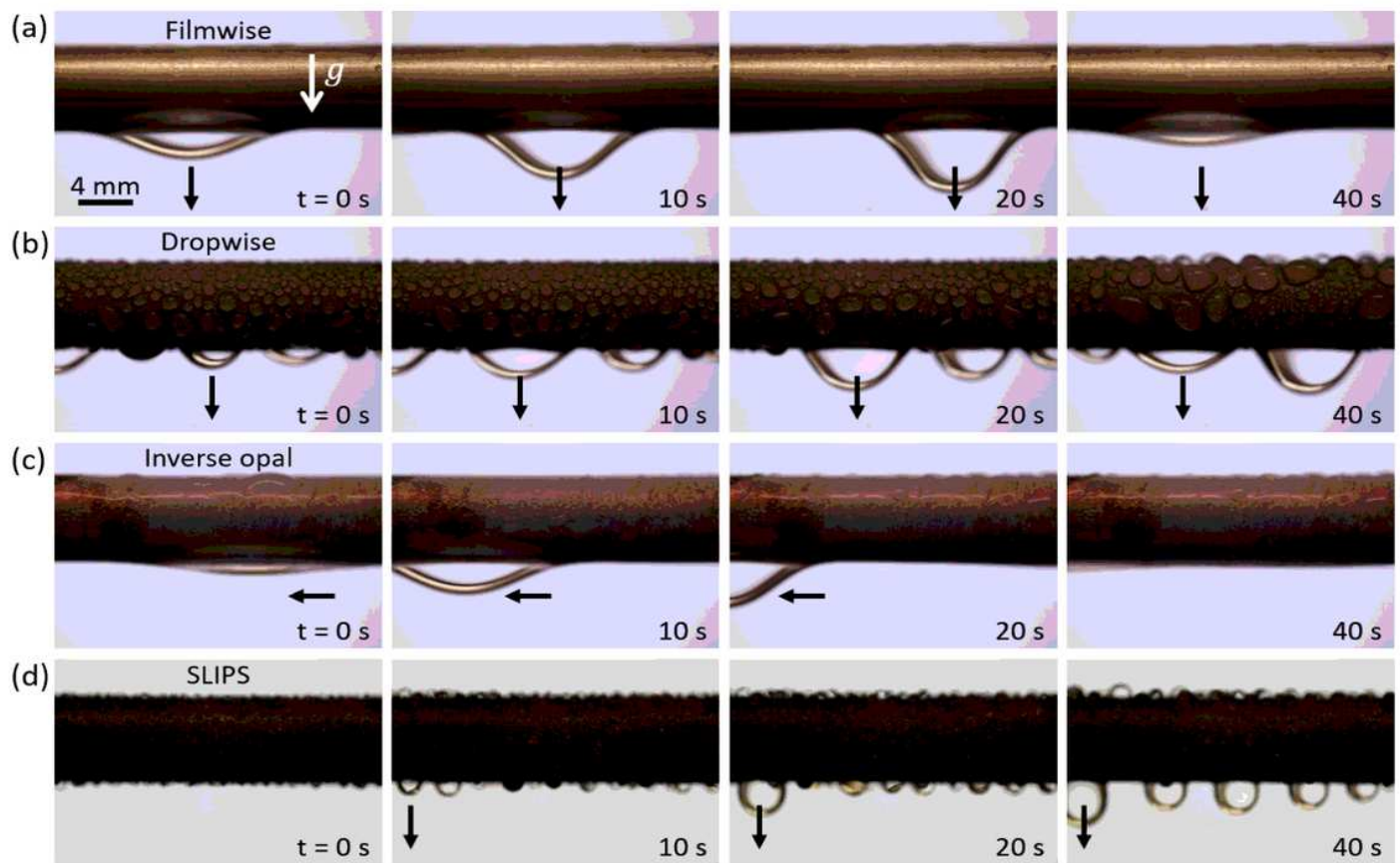


Figure 3

Modes of condensation. Time-lapse images of (a) filmwise condensation (FWC) on smooth plasma treated, (b) dropwise condensation (DWC) on smooth hydrophobized (silane treated), (c) inverse opal condensation (IOC) on silica inverse opals, and (d) SLIPS condensation on oil-impregnated silica inverse opals. In all cases except IOC, condensate was drained vertically downwards when gravity overcame pinning or surface tension forces. During IOC, however, the condensate was transported preferentially in the axial direction through the cracks (fabrication defects). Compared to nanopores, fabrication defects (cracks) provide a less-resistant flow path or high hydraulic conductivity for liquid transport.

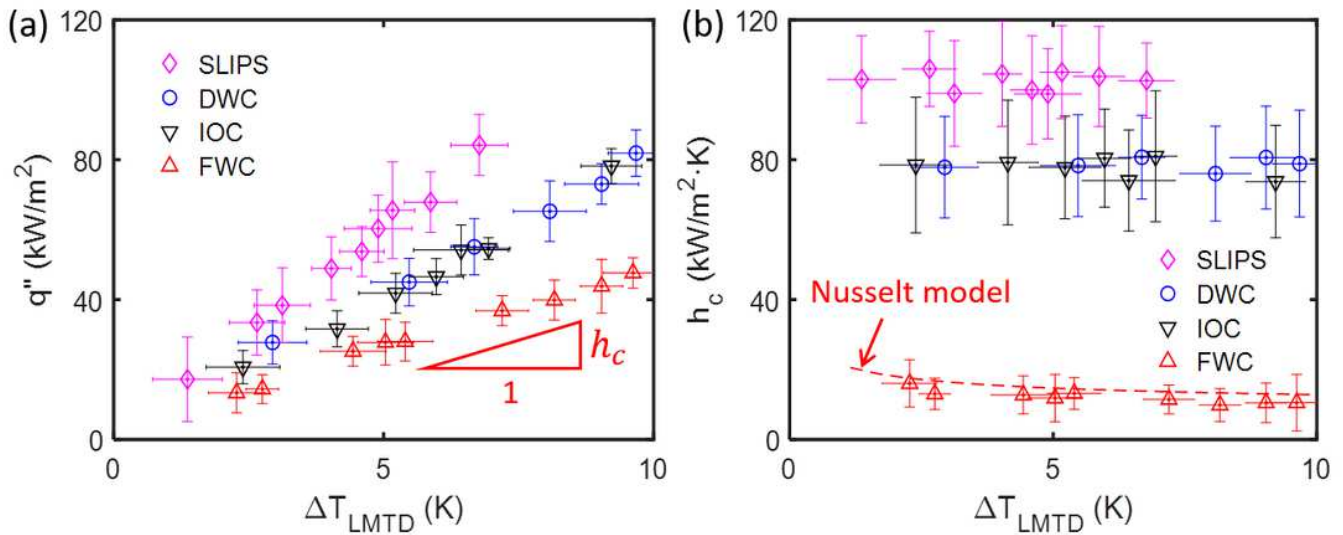


Figure 4

Heat transfer measurement. (a) Heat flux and (b) heat transfer coefficient as a function of logarithmic mean temperature difference. The slope in (a) is the heat transfer coefficient (h_c). The heat transfer coefficient for DWC and IOC are nearly identical at ~ 80 kW/m²·K; a sevenfold increase from FWC (~ 12 kW/m²·K). The heat transfer coefficient increases further by $\sim 30\%$ to ~ 103 kW/m²·K when the silica nanopores are impregnated with oil (SLIPS condensation). Our heat transfer measurements are validated by comparing the heat transfer coefficient for FWC with the classical Nusselt model for laminar film condensation (red dashed line). The error bars are obtained through standard error propagation analysis.

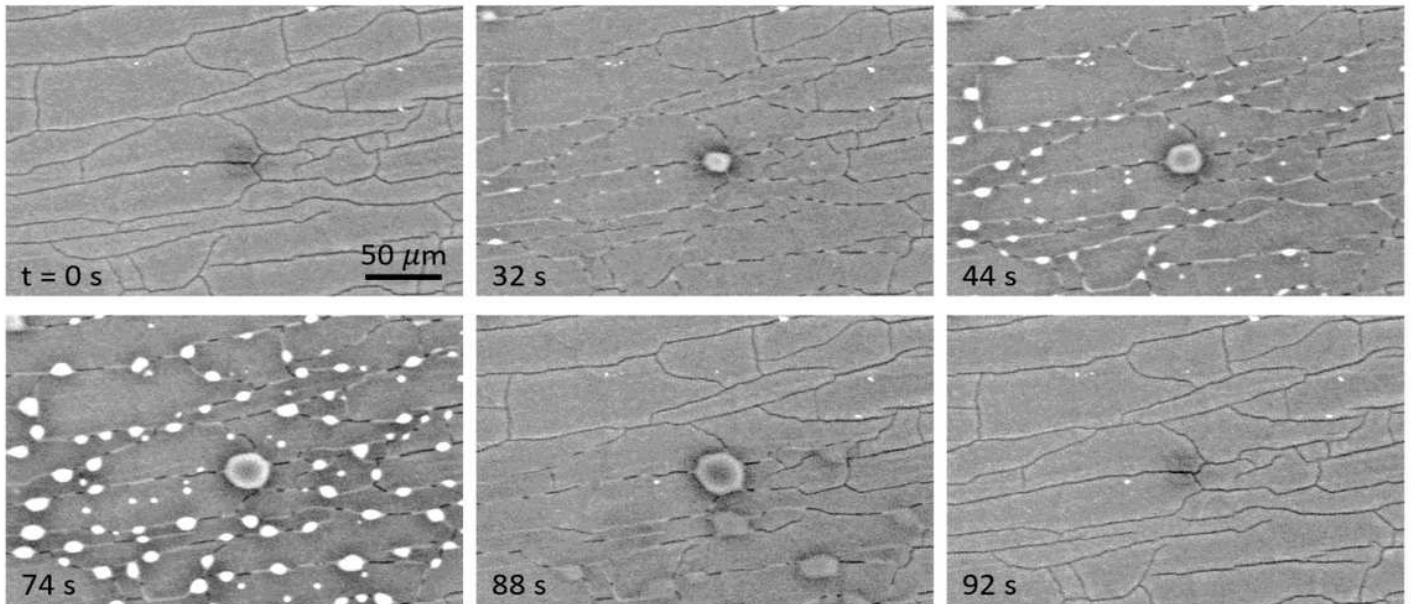


Figure 5

Environmental SEM. The ESEM was maintained at 7.4 °C and 1015 Pa. The test sample was attached to a cold stage that was subcooled by 2 °C. Time-lapse images (10 fps) show that vapor condensed preferentially near cracks (t = 32 s and 44 s). When condensation continued, the condensate overflowed (t = 74 s). The condensate was transported through the cracks (t = 88 s) and the surface dried out (t = 92 s) when vapor supply was discontinued.

Supplementary Files

This is a list of supplementary files associated with this preprint. Click to download.

- [Supportingmaterialv2.docx](#)